ACS APPLIED MATERIALS & INTERFACES

Research Article

www.acsami.org

Nanostructured (Co, Ni)-Based Compounds Coated on a Highly Conductive Three Dimensional Hollow Carbon Nanorod Array (HCNA) Scaffold for High Performance Pseudocapacitors

Lian Wan, Junwu Xiao,* Fei Xiao, and Shuai Wang*

Key Laboratory for Large-Format Battery Materials and System, Ministry of Education, Hubei Key Laboratory of Material Chemistry and Service Failure, School of Chemistry and Chemical Engineering, Huazhong University of Science & Technology, 430074 Wuhan, Hubei, PR China

Supporting Information

ABSTRACT: The electrochemical performance of the pseudocapacitive materials is seriously limited by poor electron and ions transport. Herein, an advanced integrated electrode has been designed by growing the pseudocapacitive materials, including $Co_xNi_{1-x}(OH)_2$, $Co_xNi_{1-x}O$, and $(Co_xNi_{1-x})_9S_8$, on a three-dimensional hollow carbon nanorod arrays (HCNA) scaffold. The HCNA scaffold not only can provide large surface area for increasing the mass loading of the pseudocapacitive materials, but also is with good electrical conductivity and hollow structure for facilitating fast electron and electrolyte ions transport, and thus improve the electrochemical performance. Particularly, in comparison with $Co_xNi_{1-x}(OH)_2$ and $Co_xNi_{1-x}O$ nanosheets, $(Co_xNi_{1-x})_9S_8$ nanosheets on the HCNA scaffold exhibit better electrochemical performance. The discharge areal capacitance of the $(Co_xNi_{1-x})_9S_8$/HCNA electrode can be achieved to 1.32 F cm^{-2} at 1 mA cm^{-2}, ~1.5 times as that of the $Co_xNi_{1-x}(OH)_2$/HCNA electrode. The rate capability performance is also improved. 71.8% of the capacitance is retained with increasing the discharge current density from 1 to 10 mA cm^{-2}, in contrast to ~59.9% for the $Co_xNi_{1-x}(OH)_2$/HCNA electrode. Remarkably, the cycling stability is significantly enhanced. ~111.2% of the initial capacitance is gained instead of decaying after the 3000 cycles at 8 mA cm^{-2}, while there is ~11.5% loss for the $Co_xNi_{1-x}(OH)_2$/HCNA electrode tested under the same condition. Such good electrochemical performance can be ascribed by that $(Co_xNi_{1-x})_9S_8$ exhibits the similar energy storage mechanism as $Co_xNi_{1-x}(OH)_2$ and $Co_xNi_{1-x}O$, and more importantly, is with better electrical conductivity.

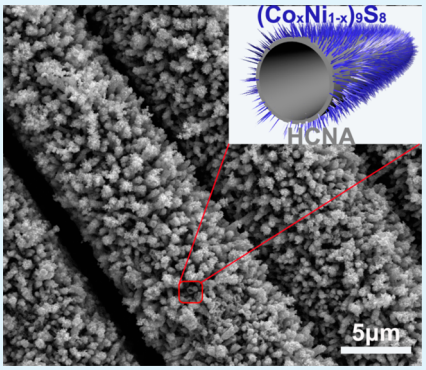

KEYWORDS: *(Co, Ni)-based compounds, hollow carbon nanorod array, ZnO nanorod array, carbon fiber paper, three-dimensional, supercapacitors*

1. INTRODUCTION

Electrochemical capacitors, also called supercapacitors, have attracted great interest because of their fast charge and discharge rate, high power density (1−2 orders of magnitude higher than lithium ion batteries), and long cycle life.[1] In general, two major types of electrochemical capacitors exist depending on the underlying energy storage mechanism: electric double-layer capacitors (EDLCs) and pseudocapacitors.[2] EDLCs store energy by the electrostatic accumulation of charges in the electric double-layer near electrode/electrolyte interfaces. However, it cannot achieve high enough energy density to meet the ever-growing need for peak-power assistance in electric vehicles. In contrast, pseudocapacitors can obviously enhance the specific capacitance and energy density by using interfacial reversible faradaic reactions to store energy.

Traditional pseudocapacitive materials mainly include transitional metal oxides/hydroxides,[2,3] such as manganese oxides,[4,5] cobalt−nickel oxides,[6,7] cobalt−nickel layered double hydroxides (LDHs),[8,9] etc. However, their conductivity is typically too low to support fast electron transport toward high rate capability. An improved method is to search for new electrode materials with good electrical conductivity and high specific performance. Transition metal sulfides, such as CoS_x, NiS_x, and $NiCo_2S_4$, are with higher electrical conductivity and quasi-energy storage mechanism as the oxides, which recently have been investigated as a new type electrode material for high performance pseudocapacitors.[10−15] However, in the preparation process of the electrodes, the polymer binder should be introduced to load the electrode materials to the current collector. Thus, the pseudocapacitive materials cannot achieve the optimal performance because of poor electron transport and long electrolyte ion diffusion paths.

To approach the optimal performance, in theory, the thickness of the pseudocapacitive materials should be infinitely small, which can ensure the complete utilization of the

Received: February 18, 2014
Accepted: April 22, 2014
Published: April 23, 2014

   dx.doi.org/10.1021/am5010199 | ACS Appl. Mater. Interfaces 2014, 6, 7735−7742

pseudocapacitive materials for energy storage because of the fast electron and electrolyte ions transport. The feasible method is to develop a three-dimensional (3D) charge conducting nanostructured scaffold for loading the active materials,[4,16−19] which owe their enhanced rate capability to the large surface area and the short diffusion paths for both electron and electrolyte ions. Carbonaceous nanomaterials are being widely explored as electrode and scaffold materials because of their low cost, low toxicity, better chemical stability, and better electrical conductivity, as compared with the ZnO,[20,21] SnO_2,[22] Zn_2SnO_4,[23] NiO,[24] H-TiO_2,[25] and $NiCo_2O_4$ 3D scaffolds.[26,27] However, in the as-reported graphene paper and hydrogel scaffold, graphene layers tend to self-aggregation because of the interlayer $\pi-\pi$ interaction, and thus decrease the surface area and inhibit electrolyte ion transport.[28−31] In addition, the fabrication processes of CNTs and graphene 3D scaffolds via chemical vapor deposition are so complex that limit their practical applications.[32−34] Herein, we report a facile method to synthesize hollow carbon nanorod arrays (HCNA) on the carbon fiber (CF) paper as a highly conductive 3D scaffold, on which (Co, Ni)-based compounds, including $Co_xNi_{1-x}(OH)_2$, $Co_xNi_{1-x}O$ and $(Co_xNi_{1-x})_9S_8$ nanosheets, are grown via a facile electrodeposition process and subsequent thermal decomposition or vulcanization process.

2. EXPERIMENTAL SECTION

2.1. Preparation of the ZnO/C Nanorod Arrays Grown on the Carbon Fiber (CF) Paper. To fabricate a three-dimensional hollow carbon nanorod arrays (HCNA) grown on the CF were prepared via a sacrificial template method. The details were described as follows: First, the ZnO nanorod arrays grown on the CF were typically prepared by the colloid pretreatment method.[35] Anhydrous zinc acetate and ethanolamine were dissolved into 2-methoxythanol. The concentrations of both ethanolamine and zinc acetate were 5 mM. The carbon fiber paper (1 cm × 2 cm) was put into the solution for 10 min, taken out, dried and annealed at 300 °C for 30 min to form the ZnO seeds. The processes were repeated for three times. Then, the carbon fiber paper containing the ZnO seeds was immersed in the 50 mM of $Zn(NO_3)_2$ and 50 mM of hexamethylenetetramine ($C_6H_{12}N_4$) solution for 12 h at 95 °C to form ZnO nanorod arrays. The carbon fiber papers with ZnO nanorod arrays are then vertically inserted into 50 mM of glucose solution, which was sealed in a Teflon-lined stainless autoclave. The Teflon-lined stainless autoclave was subsequently placed in an oven, heated to 180 °C and kept at that temperature for 12 h. After it was cooled down, the carbon fiber paper was taken off, washed with DI water, and dried. Finally, the samples were thermally treated at 700 °C under Ar atmosphere with a heating rate of 10 °C min^{-1} for 1.0 h, forming the ZnO/C heterstructured nanorod arrays on the carbon fiber paper.

2.2. Synthesis of $Co_xNi_{1-x}(OH)_2$, $Co_xNi_{1-x}O$ and $(Co_xNi_{1-x})_9S_8$ Pseudocapacitive Materials on the Hollow Carbon Nanorod Arrays (HCNA). The pseudocapacitive materials including $Co_xNi_{1-x}(OH)_2$, $Co_xNi_{1-x}O$, and $(Co_xNi_{1-x})_9S_8$ are grown on the hollow carbon nanorod arrays (HCNA) via a facile electrodeposition process and subsequent thermal decomposition or vulcanization process. The details were described as follows: First, the $Co_xNi_{1-x}(OH)_2$ precursors are formed on the ZnO/C heterstructured nanorod arrays in a standard three-electrode glass cell at 25 °C by the potential static with −1.0 V for 8 min, where the ZnO/C heterstructured nanorod arrays were as the working electrode, the saturated calomel electrode (SCE) as the reference electrode, and a Pt wire as the counter-electrode. The electrolyte was 0.1 M of $CoCl_2$ and $NiCl_2$ solution, with Ni^{2+}/Co^{2+} concentration ratio of 1:1. Then, the $Co_xNi_{1-x}(OH)_2$ precursors were transformed into the $Co_xNi_{1-x}O$ via a thermal decomposition process at 400 °C for 1.0 h under Ar atmosphere with a heating rate of 5 °C min^{-1}, and were vulcanized in 0.2 M of thioacetamide at 95 °C for 12 h to form $(Co_xNi_{1-x})_9S_8$. Finally, the ZnO nanorod templates were etched in 1.0 M KOH solution to form the $Co_xNi_{1-x}(OH)_2$/HCNA, $Co_xNi_{1-x}O$/HCNA, and $(Co_xNi_{1-x})_9S_8$/HCNA electrodes.

2.3. Characterization. The morphologies were examined by scanning electron microscopy (SEM) using NOVA NanoSEM 450 at an accelerating voltage of 10 kV. Transmission electron microscopy (TEM) observations were carried out on a FEI-Tecnai G20 U-Twin operating both at 200 kV. X-ray diffraction (XRD) was performed on a Philips PW-1830 X-ray diffractometer with Cu kα irradiation (λ = 1.5406 Å). The step size and scan rate are set as 0.05° and 0.025° s^{-1}, respectively. X-ray photoelectron spectroscopy (XPS) was measured on a PerkinElmer model PHI 5600 XPS system with a resolution of 0.3−0.5 eV from a monochromated Al anode X-ray source with Kα radiation (1486.6 eV). The electrochemical characterization was carried out in a three electrode cell, where the electroactive materials grown on the carbon fiber paper as the working electrodes, Pt foil served as the counter electrode, Hg/HgO (1.0 M KOH solution) as the reference electrode, and 1.0 M KOH aqueous solution as the electrolyte. The electrochemical capacitor performance was evaluated on a CHI 660E electrochemical workstation using cyclic voltammetry, chronopotentiometry, and A. C. impedance techniques.

3. RESULTS AND DISCUSSION

The formation process of an advanced integrated electrode designed by growing the pseudocapacitive materials on a HCNA scaffold is schematically shown in Figure 1a. First of all,

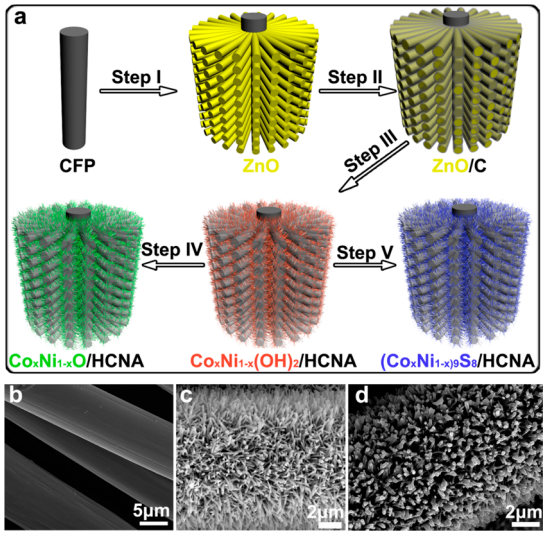

Figure 1. (a) Schematic graph of the formation process of $Co_xNi_{1-x}(OH)_2$, $Co_xNi_{1-x}O$, and $(Co_xNi_{1-x})_9S_8$ nanomaterials grown on a highly conductive hollow carbon nanotube array (HCNA) scaffold, and (b−d) SEM images of carbon fiber (CF) paper, ZnO nanorod arrays, and ZnO/C core−shell nanorod arrays grown on the carbon fiber paper.

ZnO nanorod arrays were uniformly grown and roughly vertically aligned on the smooth carbon fibers by a simple route (step I in Figure 1a), which can be seen from the XRD pattern in Supporting Information Figure S1 and SEM images in Figure 1 b and c. A thin amorphous carbon layer was then deposited on the surface of ZnO nanorods via the polymerization of glucose and subsequent thermal reduction processes (step II in Figure 1a and Figure 1d).

Co^{2+} and Ni^{2+} ions were subsequently deposited on the ZnO/C heterostructured nanorod arrays via the potential static deposition (step III in Figure 1a). After etching the ZnO nanorod templates in alkaline solution, it can be seen from the

XRD pattern the deposits are in form of $Co_xNi_{1-x}(OH)_2$, and the diffraction peaks ascribed to ZnO were not found (Supporting Information Figure S1), further revealing the complete dissolution of the ZnO nanorod templates. The $Co_xNi_{1-x}(OH)_2$ nanomaterials with nanosheet-shape are uniformly and completely covered on the surface of HCNA (Figure 2a and b). The TEM images in Figure 2c and d clearly

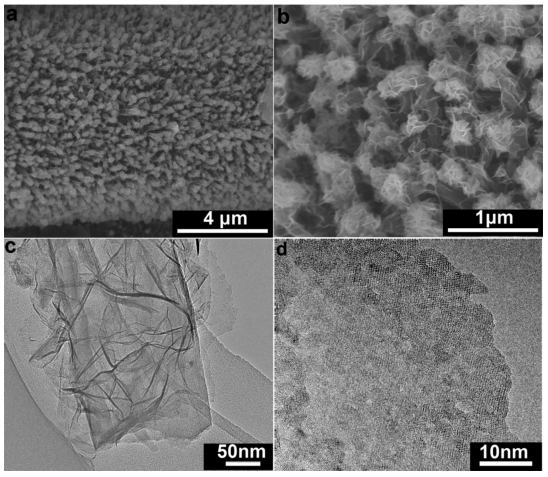

Figure 2. (a, b) SEM and (c, d) TEM images of the $Co_xNi_{1-x}(OH)_2$/HCNA electrode.

show the HCNA is with hollow structure, and $Co_xNi_{1-x}(OH)_2$ nanosheets have no porous structure. As a control, $Co_xNi_{1-x}(OH)_2$ nanosheets also can be fully grown on the surface of CF (Supporting Information Figure S2). As is well-known, HCNA grown on the CF can obviously provide larger surface area for growing $Co_xNi_{1-x}(OH)_2$ nanosheets, as compared with pristine CF. Thus, under the same electrodepositon condition, the as-formed $Co_xNi_{1-x}(OH)_2$/HCNA electrode would have higher surface area than the $Co_xNi_{1-x}(OH)_2$/CF electrode.

The $Co_xNi_{1-x}(OH)_2$ grown on the HCNA scaffold can be transformed into $Co_xNi_{1-x}O$ via the thermal decomposition process (Step IV in Figure 1a and Supporting Information Figure S1). The as-formed $Co_xNi_{1-x}O$ nanomaterials conserve the nanosheet-shape, and are completely grown on the HCNA (Figure 3a and b). As seen from Figure 3c and d, it is found that the $Co_xNi_{1-x}O$ nanosheets are with porous structure, which were formed by the water loss during the thermal treatment process. The lattice fringes with an interlayer distance of 0.24 nm in Figure 3d corresponds to the lattice fringe of the (001) crystal planes of $Co_xNi_{1-x}O$ (JCPDS 03−065−6920), in consistent with the XRD pattern.

The $Co_xNi_{1-x}(OH)_2$ nanosheets were vulcanized in the thioacetamide solution to form $(Co_xNi_{1-x})_9S_8$, of which the XRD pattern in Figure S1 is accordance with the standard pattern JCPDS 03−065−6801. The hollow structure of HCNA can be seen from the high magnification SEM image in inset of Figure 4a. The $(Co_xNi_{1-x})_9S_8$ nanomaterials are in the nanosheet-shape, just like $Co_xNi_{1-x}(OH)_2$ and $Co_xNi_{1-x}O$ nanosheets, and are completely grown on the surface of HCNA (Figure 4a−c). The corresponding TEM image in Figure 4c clearly reveals that the $(Co_xNi_{1-x})_9S_8$ nanosheets are with porous structure. The lattice fringes with an interlayer distance of 0.23, 0.25, and 0.35 nm in Figure 4d are agreement with the lattice fringe of the (331), (400) and (220) crystal planes of

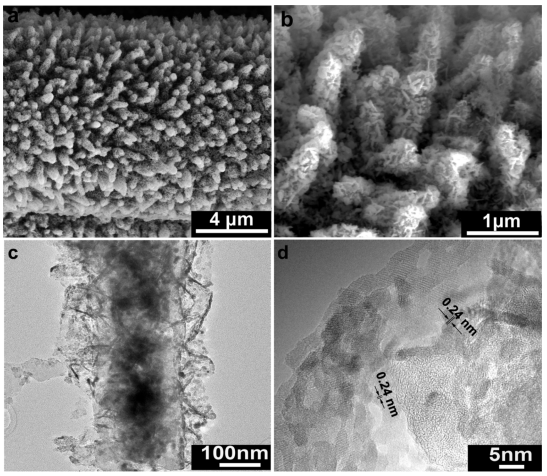

Figure 3. (a, b) SEM and (c, d) TEM images of the $Co_xNi_{1-x}O$/HCNA electrode.

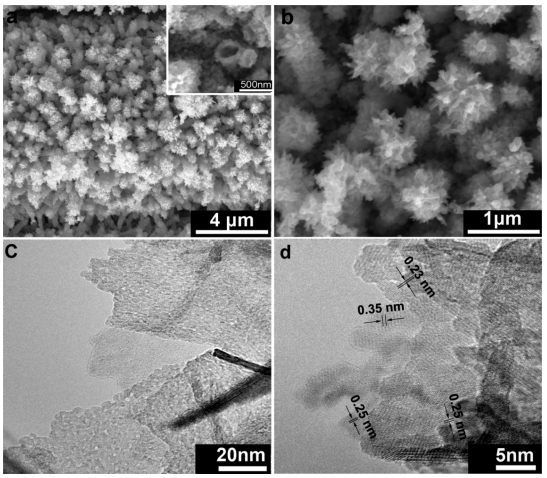

Figure 4. (a, b) SEM and (c, d) TEM images of the $(Co_xNi_{1-x})_9S_8$/HCNA electrode.

$(Co_xNi_{1-x})_9S_8$, respectively, in consistent with the XRD pattern. EDX spectrum of $(Co_xNi_{1-x})_9S_8$/HCNA in Supporting Information Figure S3 reveals that there is O element in the $(Co_xNi_{1-x})_9S_8$/HCNA composites, which should be acribed to HCNA, in consistent with XPS results discussed below. In addition, Co, Ni and S elements originate from $(Co_xNi_{1-x})_9S_8$. Cu and C elements are from Cu grid, carbon film, CF, and HCNA. Together with XRD and EDX results, it is found that $Co_xNi_{1-x}(OH)_2$ on the HCNA scaffod was completely transformed into $(Co_xNi_{1-x})_9S_8$.

To gain further information on the structure and composition of the $(Co_xNi_{1-x})_9S_8$/HCNA electrodes, we resort to X-ray photoelectron spectroscopy (XPS) measurement and the results be shown in Figure 5. The full XPS spectrum of $(Co_xNi_{1-x})_9S_8$/HCNA is presented in Figure 5a. In the C 1s spectrum (Figure 5b), the binding energies at 284.5 and 288.0 eV are corresponding to C−C and C═O, respectively. The peak at 531.5 eV in the O 1s spectrum should be ascribed to the binding energy of O−C rather than O−M (M═Co, Ni) (Figure 5c),[9] which originates from HCNA. As regards the Co 2p XPS spectrum, it shows a doublet containing a low energy band (Co $2p_{3/2}$) and a high energy band (Co $2p_{1/2}$) at 780.3 and 796.0 eV, respectively (Figure 5d). The spin−orbit splitting

dx.doi.org/10.1021/am5010199 | ACS Appl. Mater. Interfaces 2014, 6, 7735−7742

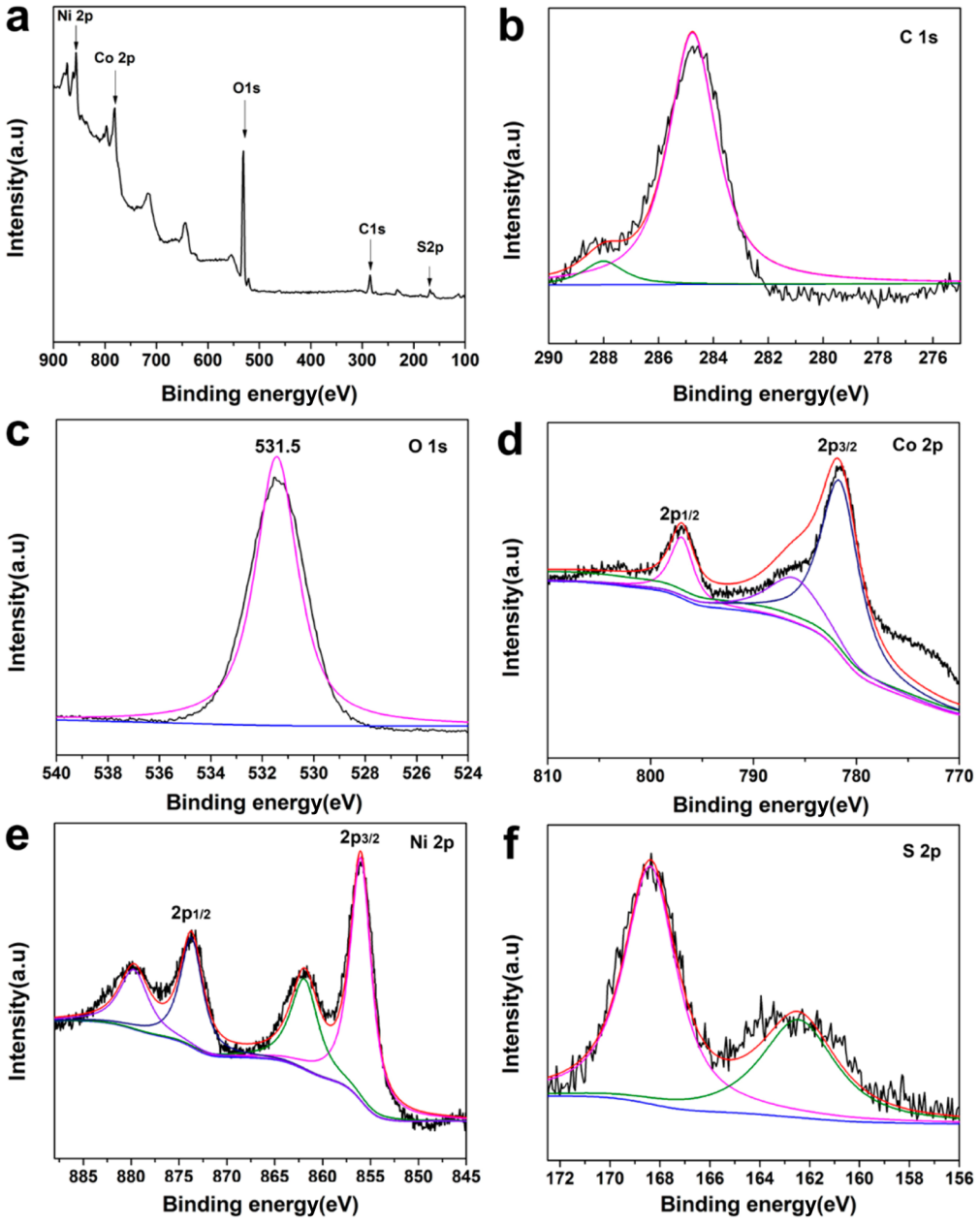

Figure 5. (a) XPS full spectra, and in the (b) C 1s, (c) O 1s, (d) Co 2p, (e) Ni 2p, and (f) S 2p regions of the $(Co_xNi_{1-x})_9S_8$/HCNA electrode.

value of Co $2p_{1/2}$ and Co $2p_{3.2}$ is over 15 eV, suggesting the coexistence of Co^{2+} and Co^{3+}.[36] Ni^{2+} is dominant in the products, as seen from that the Ni $2p_{3/2}$ peaks (855.0 eV) is close to 854.9 eV for Ni^{2+} but much lower than 857.1 eV for Ni^{3+} (Figure 5e).[37] The peak centered at ~162.0 eV in the S 2p spectrum is accordance with the binding energies of M−S (M═Co, Ni) (Figure 5f).[10] The additional peak at ~168.4 eV can be attributed to sulfur species in high oxidation state, which probably is due to the surface oxidation of $(Co_xNi_{1-x})_9S_8$.[38] The XPS results indicate that $Co_xNi_{1-x}(OH)_2$ reacted with thioacetamide to form $(Co_xNi_{1-x})_9S_8$, in consistent with the XRD and EDX results and the literatures reported previously.[39]

The electrochemical performance was then investigated in a three-electrode configuration using 1.0 M KOH electrolyte, as shown in Figure 6. Figure 6a shows the cyclic voltammogram (CV) curves at a scan rate of 5 mV s^{-1} in a potential window of 0−0.70 V. All CV curves shown here have a pair of redox peaks, different from the substantially rectangular-shaped CV curves of the ZnO, ZnO/C, and HCNA electrodes ascribed to the electric double-layer capacitance (Supporting Information Figure S4), indicating that the electrochemical performances mainly result from the pseudocapacitance. The plateaus in the galvanostatic charge/discharge curves also show the existence of Faradaic processes and the characteristic of pseudocapacitance in the electrodes (Figure 6b). As compared with that directly deposited on the CF forming the $Co_xNi_{1-x}(OH)_2$/CF electrode, the $Co_xNi_{1-x}(OH)_2$ nanosheets grown on a highly conductive HCNA scaffold under the same deposition condition exhibited a larger integrated area of CV curve, indicating higher speific capacitance. It can be ascribed by that the HCNA scaffold provided large surface area for enhancing the mass loading of $Co_xNi_{1-x}(OH)_2$, and was in favor of fast electron and electrolyte ion transport disscussed below. The $Co_xNi_{1-x}O$/HCNA and $(Co_xNi_{1-x})_9S_8$/HCNA electrodes,

dx.doi.org/10.1021/am5010199 | ACS Appl. Mater. Interfaces 2014, 6, 7735−7742

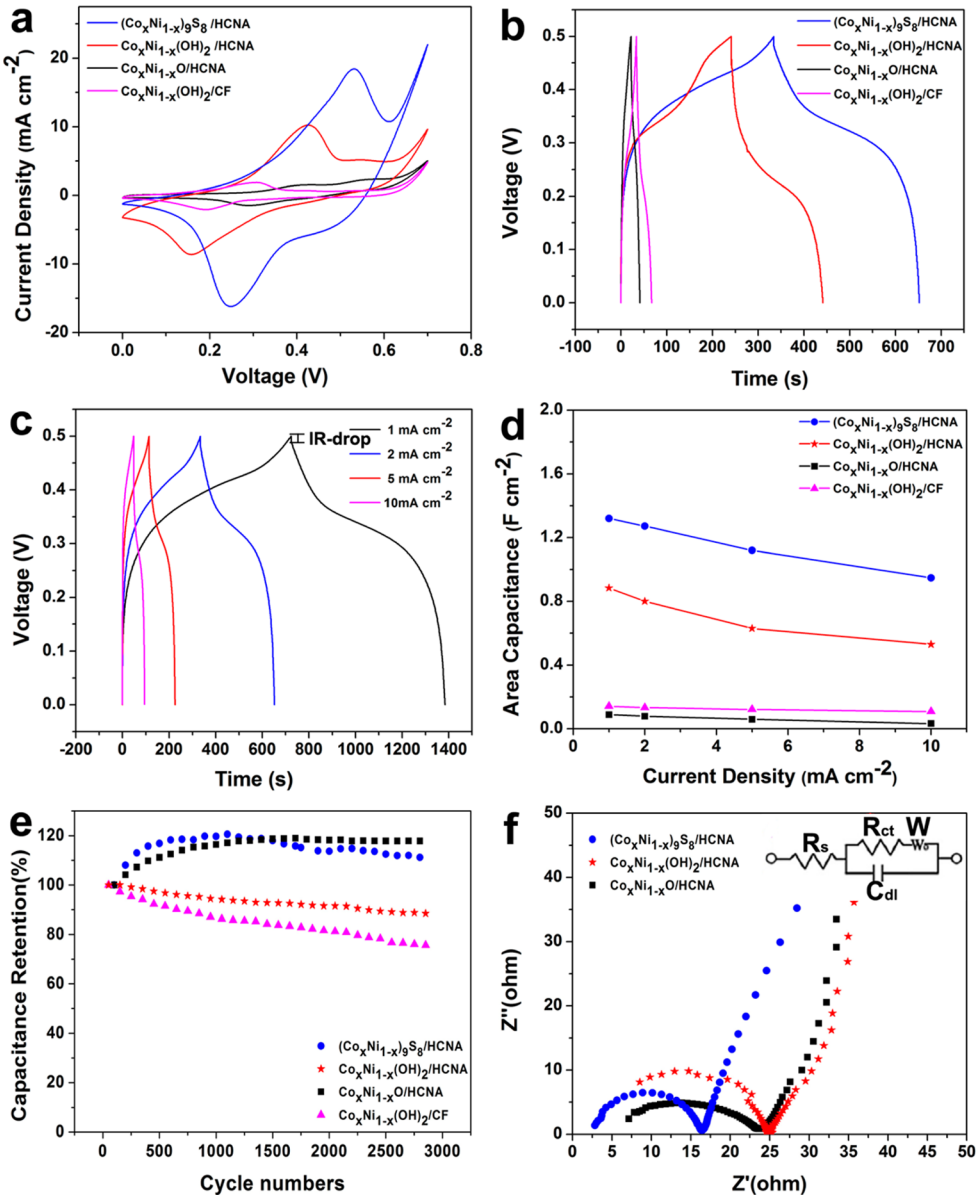

Figure 6. Electrochemical performance of the $Co_xNi_{1-x}(OH)_2$/CF, $Co_xNi_{1-x}(OH)_2$/HCNA, $Co_xNi_{1-x}O$/HCNA, and $(Co_xNi_{1-x})_9S_8$/HCNA electrodes. (a) CV curves at a scan rate of 5 mV s^{-1}. (b) Galvanostatic charge/discharge curves at a current density of 2 mA cm^{-1}. (c) Galvanostatic charge/discharge curves of the $(Co_xNi_{1-x})_9S_8$/HCNA electrode at a current density of 1, 2, 5, and 10 mA cm^{-1}. (d) Discharge areal capacitance performance. (e) Normalized specific capacitance versus cycle number at a galvanostatic charge/discharge current density of 8 mA cm^{-2}. (b) EIS Nyquist plots of the $Co_xNi_{1-x}(OH)_2$/HCNA, $Co_xNi_{1-x}O$/HCNA, and $(Co_xNi_{1-x})_9S_8$/HCNA electrodes. Inset: Equivalent circuit diagram proposed for analysis of the EIS data.

which are transformed from the $Co_xNi_{1-x}(OH)_2$/HCNA composites via the thermal decompostion and vulcanization processes, respectively, exhibit an anodic and cathodic peak. The redox peaks correspond to the redox reaction of M-O/M-OOH and M-S/M-SOH (M═Co, Ni),[6,12] respectively. According to the integrated area of CV curves, it is found that the $(Co_xNi_{1-x})_9S_8$/HCNA electrode exhibits the highest specific capacitance among the (Co, Ni)-based compounds/HCNA electrodes, in accordance with the galvanostatic charge−discharge curve shown in Figure 6b. This confirms that the $(Co_xNi_{1-x})_9S_8$ based electrode is superlative for pseudocapacitive devices.

Rate capability is a critical parameter of electrochemical capacitors for assessing the potential application, which can be seen from the symmetry and IR-drop value of the galvanostatic charge/discharge curves. Shown in Figure 6c is the representative galvanostatic charge/discharge plots of the $(Co_xNi_{1-x})_9S_8$/HCNA electrode at the current densities of 1, 2, 5, and 10 mA cm^{-2}. As compared with the $Co_xNi_{1-x}(OH)_2$/HCNA electrode, the charge/discharge curves of the $(Co_xNi_{1-x})_9S_8$/HCNA electrodes are with more symmetric (Figure 6b), and smaller IR-drop value (~10 mV) at a current density of 1 mA cm^{-2}. Even increasing to 10 mA cm^{-2}, there is less than 90 mV for the IR-drop value in the $(Co_xNi_{1-x})_9S_8$/HCNA electrode, much smaller than that in the $Co_xNi_{1-x}(OH)_2$/HCNA electrode (~190 mV). Thus, the $(Co_xNi_{1-x})_9S_8$/HCNA electrode has a better rate capability characteristic and superior reversible redox reaction, as compared with the $Co_xNi_{1-x}(OH)_2$/HCNA electrode.

dx.doi.org/10.1021/am5010199 | ACS Appl. Mater. Interfaces 2014, 6, 7735−7742

The discharge areal capacitance performance calculated from the galvanostatic charge/discharge curves is shown in Figure 6d. The discharge areal capacitance of the $Co_xNi_{1-x}(OH)_2$/CF electrode is 0.14 F cm^{-2} at 1 mA cm^{-2}. While the $Co_xNi_{1-x}(OH)_2$/HCNA electrode formed under the same electrodeposition condition as the $Co_xNi_{1-x}(OH)_2$/CF electrode, achieved the discharge areal capacitance to 0.88 F cm^{-2} at 1 mA cm^{-2}. As compared with the $Co_xNi_{1-x}(OH)_2$/CF electrode, the improvement of the capacitive performance for $Co_xNi_{1-x}(OH)_2$ formed on the HCNA under the same electrodeposition condition can be contributed by that the HCNA scaffold with large surface area enhanced the mass loading of $Co_xNi_{1-x}(OH)_2$, and facilitated electron and electrolyte ion diffusion, just like $NiCo_2O_4$ arrays in the $Co_xNi_{1-x}(OH)_2/NiCo_2O_4$ electrode.[26] However, the $Co_xNi_{1-x}(OH)_2$/HCNA electrode exhibited lower discharge areal capacitance than the $Co_xNi_{1-x}(OH)_2/NiCo_2O_4$ electrode. It can be ascribed by that the component HCNA exhibited lower discharge areal capacitance (~4.71 mF cm^{-2} at 100 mV s^{-1}), calculated from the integrated area of CV curve (Supporting Information Figure S4), as compared with $NiCo_2O_4$ array (~0.5 F cm^{-2} at 2 mA cm^{-2}). In addition, the electrodeposition condition also can influence the capacitive performance via altering the mass loading of $Co_xNi_{1-x}(OH)_2$. $(Co_xNi_{1-x})_9S_8$ on the HCNA transformed from $Co_xNi_{1-x}(OH)_2$ can further increase the discharge areal capacitance from 0.88 to 1.32 F cm^{-2}. Even at a current density of 10 mA cm^{-2}, ~71.8% of the initial specific capacitance is retained, superior to ~59.9% for the $Co_xNi_{1-x}(OH)_2$/HCNA electrode. Above results suggest that the $(Co_xNi_{1-x})_9S_8$/HCNA electrode showed higher specific capacitance and better rate capability performance than the $Co_xNi_{1-x}(OH)_2$/HCNA electrode, may since $(Co_xNi_{1-x})_9S_8$ is with better electrical conductivity,[10,13] which is also seen from the charge transfer resistance (R_{ct}) below, and with mesoporous structure for facilitating the electrolyte ion diffusion.

Cycle stability is another key parameter in relation to the performance of a supercapacitor, and was tested at a charge−discharge current density of 8 mA cm^{-2} in the potential range of 0 to 0.5 V for 3000 cycles, as shown in Figure 6e. The $Co_xNi_{1-x}(OH)_2$/CF electrodes exhibited poor cycling life, ~24.4% loss after 3000 cycles. After $Co_xNi_{1-x}(OH)_2$ was grown on a highly conducting HCNA scaffold under the same electrodeposition process, the cycling stability of the as-formed $Co_xNi_{1-x}(OH)_2$/HCNA electrode have slightly improved, ~11.5% loss after 3000 repetitive cycles, since the HCNA scaffold enhances the electron transport from the electrode/electrolyte interface. In comparison with that deposited on the $NiCo_2O_4$ nanorod arrays, in which over 18.7% of the initial specifc capacitance was lost after 2000 cycles,[26] $Co_xNi_{1-x}(OH)_2$ grown on the HCNA can show better cycle stability performance due to better structural stability and electron transport of HCNA. After transforming $Co_xNi_{1-x}(OH)_2$ to $Co_xNi_{1-x}O$ and $(Co_xNi_{1-x})_9S_8$ on a HCNA scaffold, the cycle stability performance is significantly improved. The specific capacitances have slightly increased in the initial several cycles, perhaps due to self-activation process, corresponding to the redox reaction of $Co_xNi_{1-x}O$ and $(Co_xNi_{1-x})_9S_8$ to $Co_xNi_{1-x}OOH$ and $Co_xNi_{1-x}SOH$.[12,15,40,41] Even after 3000 repetitive cycles, the specific capacitance for the $Co_xNi_{1-x}O$/HCNA and $Co_xNi_{1-x}S$/HCNA electrodes almost has no loss. The improvement of the cycle stability performance is mainly ascribed to good electrical conductivity and structure stability of the pseudocapacitive materials themselves.

To further understand the electrochemical performance characteristics, we resorted to electrochemical impedance spectroscopy (EIS) carried out at open circuit potential with an ac perturbation of 5 mV in the frequency range of 1000 kHz-0.01 Hz. Figure 6f shows the Nyquist plots thus obtained. The EIS data was fitted based on an equivalent circuit model consisting of bulk solution resistance (R_s), charge-transfer resistance (R_{ct}), double-layer capacitance (C_{dl}), and Warburg resistance (W), and the result is shown in inset of Figure 6f. Notice that the charge-transfer resistance R_{ct}, also called Faraday resistance, is a limiting factor for the specific power of a supercapacitor,[23] hence low Faraday resistance really means a high specific power achievable. The R_{ct} values are in sequence of $(Co_xNi_{1-x})_9S_8$/HCNA (12.9 Ω) < $Co_xNi_{1-x}O$/HCNA (13.3 Ω) < $Co_xNi_{1-x}(OH)_2$/HCNA (19.8 Ω). To recap, the results clearly demonstrate the advantages of combining $(Co_xNi_{1-x})_9S_8$ for energy storage and a highly conducting HCNA scaffold for electron and ions transport in the hierarchical nanostructured materials. The double-layer capacitance (C_{dl}) is closely related to the surface area of electrode materials.[34,37] As seen from EIS data, the $(Co_xNi_{1-x})_9S_8$/HCNA (1.32×10^{-7} F) and $Co_xNi_{1-x}O$/HCNA (1.38×10^{-7} F) electrodes have larger C_{dl} value, indicating higher surface area, as compared with the $Co_xNi_{1-x}(OH)_2$/HCNA electrode (2.05×10^{-8} F). It can be ascribed to forming $Co_xNi_{1-x}O$ and $(Co_xNi_{1-x})_9S_8$ porous nanosheets to increase the surface area after the thermal deocomposition and vulcanization processes, as seen from Figures 3d and 4c.

The energy and power densities are also the important parameters related to the performance of supercapacitors. Energy density is the ability to store energy and it determines how long the supercapacitors can act as a power source. Power density is the rate of energy transfer per unit volume, area or mass and it determines how fast the energy could be discharged or charged. The energy and power densities of the (Co, Ni)-based compounds/HCNA based supercapacitors under different operating conditions are calculated, and shown in Supporting Information Figure S5. It is found that the $(Co_xNi_{1-x})_9S_8$/HCNA electrode can deliver the areal energy density of 8.2 μWh cm^{-2} at a power density of 1.25 mW cm^{-2}, much higher than that of $Co_xNi_{1-x}(OH)_2$/HCNA (4.6 μWh cm^{-2}), $Co_xNi_{1-x}(OH)_2$/CF (0.9 μWh cm^{-2}), and $Co_xNi_{1-x}O$/HCNA (0.3 μW cm^{-2}) electrodes. These results are also superior to those reported for TiN nanowire arrays (4 μWh cm^{-2}),[42] and MnO_2 coated on hydrogenated-ZnO nanowire arrays (3.2 μWh cm^{-2}).[43]

Although (Co, Ni)-based compounds are with high theoretical specific capacitance, the poor electron and electrolyte ion transport results in poor electrochemical performance, and thus limit the wide application for supercapacitors. To improve the behavior of electron and electrolyte ion transport, (Co, Ni)-based compounds are deposited on a 3D HCNA scaffold. The as-formed (Co, Ni)-based compounds/HCNA electrodes exhibited superior electrochemical performance, which is attributed to the following unique features. On one hand, as compared with that directly deposited on the CF, (Co, Ni)-based compounds formed on the HCNA scaffold can be in favor of fast electron transport from the electrode/electrolyte interface. More importantly, the as-formed HCNA scaffold exhibits higher electrical conductivity than the oxide scaffolds reported previously,[20−23,26] such as, ZnO, which can be seen

from the charge transfer resistance R_{ct} of the ZnO (10.1 Ω) and ZnO/C (2.8 Ω) nanorod arrays in Supporting Information Figure S6. On the other hand, the HCNA scaffold is with large surface area for increasing the mass loading of (Co, Ni)-based compounds, and is with hollow structure for shortening electrolyte ion diffusion paths. Thus, (Co, Ni)-based compounds deposited on the HCNA scaffold can show superior electrochemical performance. In addition, as compared with $Co_xNi_{1-x}(OH)_2$/HCNA and $Co_xNi_{1-x}O$/HCNA electrodes, the $(Co_xNi_{1-x})_9S_8$/HCNA electrode can further enhance the electrochemical property for supercapacitors, which may be ascribed to the structural and electrically conductive features of $(Co_xNi_{1-x})_9S_8$. First of all, $(Co_xNi_{1-x})_9S_8$ not only has the similar energy storage mechanism as $Co_xNi_{1-x}O$ and $Co_xNi_{1-x}(OH)_2$, but also is with the porous structure to provide more electroactive sites for energy storage, as seen from C_{dl} value. Second, $(Co_xNi_{1-x})_9S_8$ is with higher electrical conductivity than $Co_xNi_{1-x}O$ and $Co_xNi_{1-x}(OH)_2$, which promotes the charge transportation, as seen from R_{ct} value. Thus, integrating the synergistic contribution of $(Co_xNi_{1-x})_9S_8$ and a highly conducting HCNA scaffold, the as-formed $(Co_xNi_{1-x})_9S_8$/HCNA electrode achieves the best electrochemical performance among the (Co, Ni)-based compounds/HCNA electrodes.

4. CONCLUSIONS

In summary, we report a highly conductive 3D HCNA as the scaffold for loading the pseudocapacitive materials including $Co_xNi_{1-x}(OH)_2$, $Co_xNi_{1-x}O$, and $(Co_xNi_{1-x})_9S_8$ for high performance supercapacitors. The HCNA scaffold has excellent chemical stability, and thus is suitable for the different pH environments of the electrolytes. More importantly, the HCNA scaffold is with large surface area for increasing the mass loading of the pseudocapacitive materials, and with hollow structure and good electrical conductivity for facilitating electrolyte ion and electron transport. As compared with $Co_xNi_{1-x}(OH)_2$ and $Co_xNi_{1-x}O$ nanosheets, $(Co_xNi_{1-x})_9S_8$ nanosheets grown on the HCNA can achieve better electrochemical performance, high to 1.32 F cm^{-2} at 1 mA cm^{-2}, 71.8% of the retention ratio with increasing the current density from 1 to 10 mA cm^{-2}, and no decay during the 3000 repetitive cycles. Such high electrochemical capacitor performance should be ascribed by that $(Co_xNi_{1-x})_9S_8$ not only has the rich redox reaction for energy storage, in much the same way as $Co_xNi_{1-x}(OH)_2$ and $Co_xNi_{1-x}O$, but also is with better electrical conductivity and mesoporous structure in favor of electron and electrolyte ions transport. We anticipate that such a designer hierarchical architecture will be applicable to more extensive hybrid materials and energy storage and conversion devices such as lithium ion batteries, water splitting cells, and photodetectors.

■ ASSOCIATED CONTENT

Supporting Information

XRD patterns of the ZnO/C, $Co_xNi_{1-x}(OH)_2$/HCNA, $Co_xNi_{1-x}O$/HCNA, and $(Co_xNi_{1-x})_9S_8$/HCNA electrpdes, SEM images of $Co_xNi_{1-x}(OH)_2$/CF. EDX spectrum of $(Co_xNi_{1-x})_9S_8$/HCNA, Ragone plots of energy vs power density of the $Co_xNi_{1-x}(OH)_2$/CF, $Co_xNi_{1-x}(OH)_2$/HCNA, $Co_xNi_{1-x}O$/HCNA, and $(Co_xNi_{1-x})_9S_8$/HCNA electrodes, CV curves and EIS Nyquist plots of ZnO and ZnO/C nanorod arrays. This material is available free of charge via the Internet at http://pubs.acs.org/.

■ AUTHOR INFORMATION

Corresponding Authors

*E-mail: chjwxiao@hust.edu.cn.
*E-mail: chmsamuel@hust.edu.cn.

Notes

The authors declare no competing financial interest.

■ ACKNOWLEDGMENTS

The research was supported by National Natural Science Foundation of China (project no. 51173055), the Fundamental Research Funds for the Central Universities (2013QN158), and Research Fund for the Doctoral Program of Higher Education of China (20130142120024).

■ REFERENCES

(1) Conway, B. E. *Electrochemical Supercapacitors: Scientific Fundamentals and Technological Application*; Plenum: New York, 1999.
(2) Simon, P.; Gogotsi, Y. Materials for Electrochemical Capacitors. *Nat. Mater.* **2008**, *7*, 845−854.
(3) Arico, A. S.; Bruce, P.; Scrosati, B.; Tarascon, J. M.; Van Schalkwijk, W. Nanostructured Materials for Advanced Energy Conversion and Storage Devices. *Nat. Mater.* **2005**, *4*, 366−377.
(4) Xiao, J.; Yang, S.; Wan, L.; Xiao, F.; Wang, S. Electrodeposition of Manganese Oxide Nanosheets on a Continuous Three-Dimensional Nickel Porous Scaffold for High Performance Electrochemical Capacitors. *J. Power Sources* **2014**, *245*, 1027−1034.
(5) Hu, C. C.; Hung, C. Y.; Chang, K. H.; Yang, Y. L. A Hierarchical Nanostructure Consisting of Amorphous MnO_2, Mn_3O_4 Nanocrystallites, and Single-Crystalline MnOOH Nanowires for Supercapacitors. *J. Power Sources* **2011**, *196*, 847−850.
(6) Xiao, J.; Yang, S. Bio-Inspired Synthesis of NaCl-Type $Co_xNi_{1-x}O$ ($0 \le x < 1$) Nanorods on Reduced Graphene Oxide Sheets and Screening for Asymmetric Electrochemical Capacitors. *J. Mater. Chem.* **2012**, No. 22, 12253−12262.
(7) Xiao, J.; Yang, S. Sequential Crystallization of Sea-Urchin-like Bimetallic (Ni, Co) Carbonate Hydroxide and Its Morphology Conserved Conversion to Porous $NiCo_2O_4$ Spinel for Pseudocapacitors. *RSC Adv.* **2011**, *1*, 588−595.
(8) Wang, H.; Casalongue, H. S.; Liang, Y.; Dai, H. $Ni(OH)_2$ Nanoplates Grown on Graphene as Advanced Electrochemical Pseudocapacitor Materials. *J. Am. Chem. Soc.* **2010**, *132*, 7472−7477.
(9) Xiao, J.; Yang, S. Nanocomposites of $Ni(OH)_2$/Reduced Graphene Oxides with Controllable Composition, Size, and Morphology: Performance Variations as Pseudocapacitor Electrodes. *ChemPlusChem.* **2012**, *77*, 807−816.
(10) Pu, J.; Wang, Z.; Wu, K.; Yu, N.; Sheng, E. Co_9S_8 Nanotube Arrays Supported on Nickel Foam for High-Performance Supercapacitors. *Phys. Chem. Chem. Phys.* **2014**, *16*, 785−791.
(11) Yang, J.; Duan, X.; Qin, Q.; Zheng, W. Solvothermal Synthesis of Hierarchical Flower-Like β-NiS With Excellent Electrochemical Performance for Supercapacitors. *J. Mater. Chem. A* **2013**, *1*, 7880−7884.
(12) Zhang, L.; Wu, H. B.; Lou, X. W. Unusual CoS_2 Ellipsoids With Anisotropic Tube-Like Cavities and Their Application in Supercapacitors. *Chem. Commun.* **2012**, *48*, 6912−6914.
(13) Chen, H.; Jiang, J.; Zhang, L.; Wan, H.; Qi, T.; Xia, D. Highly Conductive $NiCo_2S_4$ Urchin-Like Nanostructures for High-rate Pseudocapacitors. *Nanoscale* **2013**, *5*, 8879−8883.
(14) Peng, S.; Li, L.; Li, C.; Tan, H.; Cai, R.; Yu, H.; Mhaisalkar, S.; Srinivasan, M.; Ramakrishna, S.; Yan, Q. In Situ Growth of $NiCo_2S_4$ Nanosheets on Graphene for High-Performance Supercapacitors. *Chem. Commun.* **2013**, *49*, 10178−10180.
(15) Xiao, J.; Wan, L.; Yang, S.; Xiao, F.; Wang, S. Design Hierarchical Electrodes with Highly Conductive $NiCo_2S_4$ Nanotube Arrays Grown on Carbon Fiber Paper for High-Performance Pseudocapacitors. *Nano Lett.* **2014**, *14*, 831−838.

(16) Lang, X.; Hirata, A.; Fujita, T.; Chen, M. Nanoporous Metal/Oxide Hybrid Electrodes for Electrochemical Supercapacitors. *Nat. Nanotechnol.* **2011**, *6*, 232−236.
(17) Zhang, H.; Yu, X.; Braun, P. V. Three-dimensional Bicontinuous Ultrafast-Charge and -Discharge Bulk Battery Electrodes. *Nat. Nanotechnol.* **2011**, *6*, 277−281.
(18) Qian, L. H.; Das, B.; Li, Y.; Yang, Z. Giant Raman Enhancement on Nanoporous Gold Film by Conjugating with Nanoparticles for Single-Molecule Detection. *J. Mater. Chem.* **2010**, *20*, 6891−6895.
(19) Qian, L. H.; Ding, Y.; Fujita, T.; Chen, M. W. Synthesis and Optical Properties of Three-Dimensional Porous Core-Shell nano-architectures. *Langmuir* **2008**, *24*, 4426−4429.
(20) He, Y. B.; Li, G. R.; Wang, Z. L.; Su, C. Y.; Tong, Y. X. Single-Crystal ZnO Nanorod/Amorphous and Nanoporous Metal Oxide Shell Composites: Controllable Electrochemical Synthesis and Enhanced Supercapacitor Performances. *Energy Environ. Sci.* **2011**, *4*, 1288−1292.
(21) Xia, X.; Tu, J.; Zhang, Y.; Wang, X.; Gu, C.; Zhao, X. B.; Fan, H. J. High-Quality Metal Oxide Core/Shell Nanowire Arrays on Conductive Substrates for Electrochemical Energy Storage. *ACS Nano* **2012**, *6*, 5531−5538.
(22) Li, R.; Ren, X.; Zhang, F.; Du, C.; Liu, J. Synthesis of Fe_3O_4@SnO_2 Core-Shell Nanorod Film and Its Application as a Thin-film Supercapacitor Electrode. *Chem. Commun.* **2012**, *48*, 5010−5012.
(23) Bao, L. H.; Zang, J. F.; Li, X. D. Flexible Zn_2SnO_4/MnO_2 Core/Shell Nanocable−Carbon Microfiber Hybrid Composites for High-Performance Supercapacitor Electrodes. *Nano Lett.* **2011**, *11*, 1215−1220.
(24) Liu, J.; Jiang, J.; Bosman, M.; Fan, H. J. Three-Dimensional Tubular Arrays of MnO_2-NiO Nanoflakes with High Areal Pseudocapacitance. *J. Mater. Chem.* **2012**, *22*, 2419−2426.
(25) Lu, X.; Yu, M.; Wang, G.; Zhai, T.; Xie, S.; Ling, Y.; Tong, Y.; Li, Y. H-TiO_2@MnO_2//H-TiO_2@C Core-Shell Nanowires for High Performance and Flexible Asymmetric Supercapacitors. *Adv. Mater.* **2013**, *25*, 267−272.
(26) Huang, L.; Chen, D.; Ding, Y.; Feng, S.; Wang, Z. L.; Liu, M. Nickel-Cobalt Hydroxide Nanosheets Coated on $NiCo_2O_4$ Nanowires Grown on Carbon Fiber Paper for High-Performance Pseudocapacitors. *Nano Lett.* **2013**, *13*, 3135−3139.
(27) Yu, L.; Zhang, G.; Yuan, C.; Lou, X. W. Hierarchical $NiCo_2O_4$@MnO_2 Core−Shell Heterostructured Nanowire Arrays on Ni Foam as High-Performance Supercapacitor Electrodes. *Chem. Commun.* **2013**, *49*, 137−139.
(28) Wu, Q.; Xu, Y.; Yao, Z.; Liu, A.; Shi, G. Supercapacitors Based on Flexible Graphene/Polyaniline Nanofiber Composite Films. *ACS Nano* **2010**, *4*, 1963−1970.
(29) Xu, Y.; Sheng, K.; Li, C.; Shi, G. Self-Assembled Graphene Hydrogel via a One-Step Hydrothermal Process. *ACS Nano* **2010**, *4*, 4324−4330.
(30) Chen, J.; Li, C.; Shi, G. Graphene Materials for Electrochemical Capacitors. *J. Phys. Chem. Lett.* **2013**, *4*, 1244−1253.
(31) Xu, D.; Xu, Q.; Wang, K.; Chen, J.; Chen, Z. Fabrication of Free-Standing Hierarchical Carbon Nanofiber/Graphene Oxide/Polyaniline Films for Supercapacitors. *ACS Appl. Mater. Interfaces* **2013**, *6*, 200−209.
(32) Li, N.; Chen, Z.; Ren, W.; Li, F.; Cheng, H. M. Flexible Graphene-Based Lithium Ion Batteries with Ultrafast Charge and Discharge Rates. *Proc. Natl. Acad. Sci. U. S. A.* **2012**, *109*, 17360−17365.
(33) Zhang, H.; Cao, G.; Yang, Y. Carbon Nanotube Arrays and Their Composites for Electrochemical Capacitors and Lithium-Ion Batteries. *Energy Environ. Sci.* **2009**, *2*, 932−943.
(34) Mazloumi, M.; Shadmehr, S.; Rangom, Y.; Nazar, L. F.; Tang, X. Fabrication of Three-Dimensional Carbon Nanotube and Metal Oxide Hybrid Mesoporous Architectures. *ACS Nano* **2013**, *7*, 4281−4288.
(35) Guo, M.; Diao, P.; Cai, S. M. Hydrothermal Growth of Well-Aligned ZnO Nanorod Arrays: Dependence of Morphology and Alignment Ordering upon Preparing Conditions. *J. Solid State Chem.* **2005**, *178*, 1864−1873.
(36) Xiao, J. W.; Zeng, X. W.; Chen, W.; Xiao, F.; Wang, S. High Electrocatalytic Activity of Self-Standing Hollow $NiCo_2S_4$ Single Crystalline Nanorod Arrays towards Sulfide Redox Shuttles in Quantum Dot-Sensitized Solar Cells. *Chem. Commun.* **2013**, *49*, 11734−11736.
(37) Nydegger, M. W.; Couderc, G.; Langell, M. A. Surface Composition of $Co_xNi_{1-x}O$ Solid Solutions by X-Ray Photoelectron and Auger Spectroscopies. *Appl. Surf. Sci.* **1999**, *147*, 58−66.
(38) Sato, K.; Kojima, S.; Hattori, S.; Chiba, T.; Ueda-Sarson, K.; Torimoto, T.; Tachibana, Y.; Kuwabata, S. Controlling Surface Reactions of CdS Nanocrystals: Photoluminescence Activation, Photoetching, and Photostability under Light Irradiation. *Nanotechnology* **2007**, *18*, No. 465702.
(39) Mulmudi, H. K.; Batabyal, S. K.; Rao, M.; Prabhakar, R. R.; Mathews, N.; Lam, Y. M.; Mhaisalkar, S. G. Solution Processed Transition Metal Sulfides: Application as Counter Electrodes in Dye Sensitized Solar Cells (DSCs). *Phys. Chem. Chem. Phys.* **2011**, *13*, 19307−19309.
(40) Tao, F.; Zhao, Y. Q.; Zhang, G. Q.; Li, H. L. Electrochemical Characterization on Cobalt Sulfide for Electrochemical Supercapacitors. *Electrochem. Commun.* **2007**, *9*, 1282−1287.
(41) Rakhi, R. B.; Chen, W.; Cha, D.; Alshareef, H. N. Substrate Dependent Self-Organization of Mesoporous Cobalt Oxide Nanowires with Remarkable Pseudocapacitance. *Nano Lett.* **2012**, *12*, 2559−2567.
(42) Lu, X.; Wang, G.; Zhai, T.; Yu, M.; Xie, S.; Ling, Y.; Liang, C.; Tong, Y.; Li, Y. Stabilized TiN Nanowire Arrays for High-Performance and Flexible Supercapacitors. *Nano Lett.* **2012**, *12*, 5376−5381.
(43) Yang, P.; Xiao, X.; Li, Y.; Ding, Y.; Qiang, P.; Tan, X.; Mai, W.; Lin, Z.; Wu, W.; Li, T.; Jin, H.; Liu, P.; Zhou, J.; Wong, C. P.; Wang, Z. L. Hydrogenated ZnO Core-Shell Nanocables for Flexible Supercapacitors and Self-Powered Systems. *ACS Nano* **2013**, *7*, 2617−2626.